ARTICLE

Long-lived electrets and lack of ferroelectricity in methylammonium lead bromide $CH_3NH_3PbBr_3$ ferroelastic single crystals

Received 00th January 20xx,
Accepted 00th January 20xx

DOI: 10.1039/x0xx00000x

Alessandra Geddo Lehmann[a], Francesco Congiu[*a], Daniela Marongiu[a], Andrea Mura[a], Alessio Filippetti[a,b], Alessandro Mattoni[*b], Michele Saba[a], Guido Pegna[a], Valerio Sarritzu[a], Francesco Quochi[a] and Giovanni Bongiovanni[a]

Hybrid lead halides $CH_3NH_3PbX_3$ (X = I, Br, Cl) emerged as a new class of semiconductors for low cost optoelectronic devices with superior performances. Since their perovskite crystal structure may have lattice instabilities against polar distortions, they are also being considered as potential photo-ferroelectrics. However, research on their ferroelectricity has given so far inconclusive results and the subject is far from being settled. Here we investigate, by a combined experimental and theoretical approach, the possible presence of electric polarization in tetragonal and orthorhombic $CH_3NH_3PbBr_3$ (T-MAPB and O-MAPB). We found that T-MAPB does not sustain spontaneous polarization but, under an external electric field, it is projected into a metastable, ionic space-charge electret state. The electret can be frozen on cooling, producing a large and long-lasting polarization in O-MAPB. Molecular dynamics simulations show that ferroelastic domain boundaries are able to trap charges and segregate ionic point defects, so playing a favorable role in the stabilization of the electret. At low temperature, the lack of ferroelectric behavior is explained by first principle calculations as the results of the tight competition among many metastable states with randomly oriented polarization; this large configurational entropy does not allow a single polar state to dominate in any significant temperature range.

Introduction

Soon after the discovery of the lead-based hybrid perovskites $MAPbX_3$ (MA = CH_3NH_3, X = I, Br, Cl) as high-efficiency photovoltaic materials[1], a passionate debate started on their possible ferroelectric properties, which could explain their excellent light-to-electricity conversion capability.[2–4] The debate was especially alimented by the anomalous current-voltage (*I-V*) hysteresis observed in $MAPbI_3$,[5–7] initially ascribed to internal electrical fields associated to switchable polarized domains.[8,9] Nowadays the *I-V* hysteresis is mainly attributed to ion migration in forward and reversed biases,[10–14] nonetheless, ferroelectricity continued to be proposed as a key mechanism to facilitate charge separation[15,16] and suppress electron-hole recombination.[17–19]

Experiments on the subject mainly concerned the room temperature tetragonal phase of $MAPbI_3$ (T-MAPI), with inconclusive results.[10,11,20–26] The primary uncertainty derives since T-MAPI is a lossy dielectric, with prevalent ionic conductivity,[27,28] this aspect conveys spurious opening of polarization versus electric field *P*(*E*) loops[29] and non-piezoelectric, hysteretic components in piezoresponse force microscopy measurements,[30,31] thus severely complicating the interpretation of these two major experimental analyses.

Much less discussed has been the bromide counterpart $CH_3NH_3PbBr_3$ (MAPB), a potential candidate as green light-emitting diode and as top absorber in tandem solar cells.[32–37] Cubic MAPB (C-MAPB) undergoes, on cooling, a sequence of structural phase transitions that in principle might lead to polar phases. Tetragonal T-MAPB and orthorhombic O-MAPB are derived from the $Pm\bar{3}m$ cubic prototype by first order ferroelastic transitions at T_C^T = 237 K and T_C^O = 145 K.[38] An incommensurate intermediate phase exists in a narrow temperature range (145 K - 155 K).[38,39] The crystal structures of T-MAPB and O-MAPB were assigned either to polar (*I4cm* and $Pbn2_1$)[38,40] or centrosymmetric (*I4/mcm* and *Pbnm*)[41,42] space groups by different authors, with negligible differences in the refinements R-factors. In any case, MA^+ permanent dipoles are not expected to be implied in long range spontaneous polarization of order-disorder type, being antiparallel aligned in O-MAPB[39] and dynamically disordered in T-MAPB,[38,42,43]

[a] Dipartimento di Fisica, Università degli Studi di Cagliari, I-09042 Monserrato (CA), Italy.
[b] Istituto Officina dei Materiali, CNR-IOM SLACS Cagliari, Cittadella Universitaria, I-09042 Monserrato (CA), Italy.

† Electronic Supplementary Information (ESI) available: X-ray diffraction characterization, specific heat measurements, dielectric constant measurements, details about the remanent hysteresis measurements, poling of T-MAPB and O-MAPB in negative electric fields. See DOI: 10.1039/x0xx00000x

results supported by classical[44] and *ab initio*[45] molecular dynamics simulations. Ferroelectricity could instead originate, in principle, from polar modes involving ions shifts, like in tetragonal *I4cm* $(Pb_{0.5}Bi_{0.5})(Ti_{0.5}Fe_{0.5})O_3$[46] and in orthorhombic *Pbn2₁* $CdTiO_3$[47,48], as recently proposed for tetragonal $CH_3NH_3PbI_3$.[49]

In the rare articles discussing ferroelectricity in MAPB, lack of of pyroelectricity[50] and second harmonic generation[51] were reported for C-MAPB; on the other hand, spontaneous polarization in T-MAPB and O-MAPB was claimed in Ref.[52]; here peaks of thermally stimulated depolarization (or discharge) currents (TSDCs) were measured at both orthorhombic to tetragonal and tetragonal to cubic transitions, and ferroelectricity was inferred by the sign change of those currents with the reversal of the poling field. However, just like MAPI, MAPB displays mixed electronic/ionic conductivity in a wide temperature range. At standard pressure, when thermally activated ionic conductivity prevails, Br^- and MA^+ hop along migration channels under the effect of external field and accumulate at localized sites or near electrodes.[36,53] In this situation it may be challenging to distinguish a pyroelectric current related to ferroelectricity from currents due to thermal release of trapped charges, and in particular to the depolarization of those kinds of metastable states known as electrets. Electrets[54] are states of dielectric materials with a semi-permanent electric dipole.[55] They can be obtained by charging a sample through cooling in an external electric field, which causes a frozen-in alignment of permanent dipoles or real charge displacements on long distances and their trapping at interfaces. While in principle metastable, the field-induced polarized state can be so robust to last for years after the removal of the applied field, thus giving rise to a permanent (on any practical ground) source of electric field. Ferroelectrics too retain, in zero field, an electric dipole that however, at difference from electrets, is not field-induced but emerges as an order parameter of a phase transition from a paraelectric state. Thus, while a poled (i.e. single domain) ferroelectric material is an electret, electrets do not necessarily require ferroelectricity.

Widespread among organic polymers, electrets are also found in inorganic materials;[56] in the family of perovskites, they have been observed in ABO_3 oxides since the late 1980s,[57] with the magnitude of the induced electric charge strictly dependent on the concentration of intrinsic point defects, i.e. A- and O-ion vacancies. Recently, electrets persisting over a year were reported in manganese perovskites.[58] To our knowledge, in the case of $MAPbX_3$ perovskites, electret features have been mentioned only in a recent work by Wilson et al.[59] with reference to the polar behavior of the iodide, and not investigated further.

In this paper we take up the issue of ferroelectricity of the bromide compound, by using a combination of dielectric response measurements and theoretical calculations. While we do not find equilibrium ferroelectricity, evidence is provided for metastable electret states, likely associated to charged ionic point-defects, which can be frozen at low temperatures and segregated at ferroelastic domains boundaries, to give long-living polarization in the orthorhombic phase.

Methods

Experimental methods

Synthesis of single crystal. Single crystals of $CH_3NH_3PbBr_3$ were synthesized according to the inverse temperature crystallization method.[60] CH_3NH_3Br was purchased from DyeSol while $PbBr_2$ (99.999%) and the other chemicals were purchased from Sigma-Aldrich and used without further purification. $PbBr_2$ and CH_3NH_3Br were dissolved in 1:1 molar ratio in N,N-dimethylformamide (1 m solution) at room temperature. The solution temperature was thereafter increased up to 80 °C. Under these conditions, several well shaped single crystals grew within three hours.

Structural characterization and single crystal orientation. The structural characterization was performed by X-ray powder diffraction on grinded crystals, using a Bruker D8 Advance diffractometer (Cu kα radiation). Crystals orientation was obtained by specular diffraction scans using the sample stage of a Bruker D8 Discover Diffractometer for thin films.

Polarized optical microscopy. Observation of MAPBr single crystals in transmission was performed by means of a homemade polarized light microscope, with a temperature controlled sample stage kept under dynamic N_2 atmosphere.

Specific heat. The specific heat was measured with a Quantum Design physical properties measurement system (PPMS) which employs a thermal-relaxation calorimeter that operates in the temperature range of 1.8–395 K. The system exhibits an overall accuracy of better than 1% for temperatures between 100 and 300 K.

Complex dielectric constant. The complex dielectric permittivity, ε'-iε" was measured with a Keisight 4980AL LCR meter with a four-wire probe for frequency from 20 Hz to 1 MHz. Ag electrodes of defined diameter were deposited under vacuum on both faces of masked plate-shaped crystals. Gold or copper wires were soldered by silver paste on the Ag electrodes. Contacted crystals were placed in the PPMS cryostat by means of a custom modified multifunction probe. Temperature control and data acquisition was automated by a dedicated software by PolyK Technologies, LLC. AC conductivity as a function of temperature was determined from the measured complex dielectric constant. Ferroelectric loops and TSDC were measured on crystal prepared in the same way.

Ferroelectric loops. Ferroelectric characterization was performed with a Radiant Ferroelectric Precision Tester with a Radiant Precision high voltage interface and a Trek 609D-6 high voltage amplifier. Measurements were performed at different temperatures placing the crystals either in a SUN ambient chamber or in a homemade copper chamber cooled down in a Janis cryostat (SVT-300). In the SUN chamber, the sample stage was kept in inert N_2 atmosphere, while the crystals themselves were kept in an oil bath to prevent at the same time electric discharges and contact with moisture. In

the copper chamber, crystals were always kept in vacuum, while the thermal control was obtained by changing the temperature inside the cryostat. Sample temperature was setted and controlled using (1) a thermocouple placed close to the sample position, (2) an external thermocouple located in the cryostat side and (3) a copper coil controlled by an electronic driver.

Thermally stimulated depolarization current (TSDC). In TDSC experiments, crystals were cooled at a constant rate (2 K/min) in the SUN ambient chamber. During the cooling process the samples were preconditioned, according to different E_{DC} / T protocols, by a combination of DC bias and voltage pulses applied by the Radiant Tester and the Trek high voltage amplifier. At the end of the poling protocol, the thermally stimulated discharge current was measured in zero applied, field after shorting the sample, through a Keithley 6487 picoammeter while warming the sample at 5 K/min.

Computational methods

MD calculations. Classical Molecular Dynamics: The model of Σ/110 twin mirror boundaries was obtained by i) cutting an orthorhombic crystal of $MAPbBr_3$ with (110) surfaces; ii) generating a replica by a mirror-symmetry across the surface; iii) translating and merging the two crystals; and iv) applying periodic boundary conditions. The 24576-atoms model obtained by this procedure was first optimized by conjugate gradient forces minimization in a fully flexible simulation box. Vacancy (interstitials) was generated by removal (insertion) of the corresponding species (bromide or methylammonium molecule). The energy profiles were obtained by i) selecting reference atoms (Pb or Br) along a linear region orthogonal to the boundaries; ii) placing one defect close to a selected reference atom; iii) optimizing atomic positions and energy by forces minimization; and iv) repeating i)-iii) for all reference atoms and collecting all data as a function of defect position. The profile was obtained by a local running average. All simulations were performed by using the LAMMPS code.[61]

Ab initio calculations. Structural relaxations were performed by density functional theory and PBEsol exchange-correlation functional, which is typically accurate for the structural optimization of ferroelectric materials, using the Quantum Espresso package[62] implemented in plane-wave plus ultrasoft pseudopotential[63] basis set, with a cutoff energy of 35 Ry. For the orthorhombic *Pbnm* structure of MAPB we assume the 48-atom unit cell described by[42] with a = 8.565 Å, b = 7.976 Å, c = 11.841 Å. The same methodology was previously applied to the study of electronic[64] optical and recombination[65], and defect properties[66] of MAPI. The electronic polarization is calculated by the Berry phase (BP) approach[67] on an 11 k-point string along the polarization-parallel direction and 6 × 6 k-point sampling in the orthogonal plane.

Results and discussion

Hereafter, we present polarization vs electric field loops $P(E)$ of as-grown and poled MAPB single crystals, the characterization of which is reported in the Supplementary Information **(Fig. S1-S3)**. For MAPB, resistive non-hysteretic components - rapidly relaxing to zero when the field is removed - will contribute to the total $P(E)$ loop and must be subtracted. In the following, $P_R(E)$ will indicate hysteresis obtained by "remanent polarization" measuring task implemented in the herewith used Radiant Tester. This task discriminates non-hysteretic polarization components and it extracts $P_R(E)$, which is the quantity of more interest, and the associated instantaneous current $I_R(E)$ authomatically,[68,69] as described in details in Supporting Information **S4**.

Unpoled crystals. The $P(E)$ loop of as-grown MAPB single crystals cooled from 300 K to 4 K measured in a moderate alternate electric field E_{AC} = 2.5 kV/cm, applied along the cubic direction $[001]_C$, is shown in **Fig. 1a**. The loop is cigar-shaped as commonly observed for lossy dielectrics exhibiting both permittivity and conductivity.[70] The systematic modification of the loop shape indicates gradual transformation from a tetragonal lossy dielectric to an orthorhombic linear capacitor, with a sudden loop closure at T_C^O. This process reflects the step-like suppression of the thermally activated hopping conductivity of T-MAPB at the tetragonal to orthorhombic transition. This is shown in **Fig. 1b**, that displays the temperature variation of the low frequency AC conductivity $\sigma_{AC}(T)$ obtained from the imaginary part of the dielectric constant $\varepsilon''(T)$ as $\sigma_{AC}(T) = 2\pi\nu\varepsilon_0\varepsilon''(T)$ for 60 Hz < ν < 100 Hz. The activation energy E_A for conduction in T-MAPB can be determined from the modified Arrhenius plot of the expression $\sigma_{AC}(T) = (\sigma_0/T) \times \exp(-E_A/k_BT)$ (**Fig. 1c**) (verified theoretically in hybrid perovskites[71]), where σ_0 is the pre-exponential factor, k_B is the Boltzmann constant, and T the absolute temperature.[27] The obtained E_A = 120 meV, nearly constant for the shown frequency range, is consistent with the high mobility of ionic defects expected in metal halides[14,71] and not too far from previously reported values for hopping of both Br^- and MA^+ by DC conductivity.[12,72]

Back to the $P(E)$ loops of **Fig. 1a**, at different temperatures below T_C^O the measuring field E_{AC} was slowly increased to verify if ferroelectric domain switching could be induced in unpoled O-MAPB or if an antiferroelectric double loop could at last be obtained. Neither of these situations occurred: the $P(E)$ loop only acquired weak lossy character (not shown), while no switching was observed up to the highest electric field the crystal/contacts system could sustain.

In the attempt to promote in O-MAPB domain switching through nucleation and growth, square pulses of electric field with larger amplitude than the aforementioned limit value were applied to the crystals. We tested different temperatures below T_C^O and we show in **Fig. 1d**, **e** the resulting $P_R(E)$ loops at the two extreme ones (4 K and 120 K), after two 25 kV/cm pulses of 0.5 seconds. While being open, $P_R(E)$ loops of O-MAPB after electric field pulses still lack the second essential condition for ferroelectricity, i.e. clear polarization switching, marked by positive and negative current peaks in $I_R(E)$ (for positive and negative applied field respectively) in correspondence of the coercive field $\pm E_c$. The $I_R(E)$ loop of **Fig.**

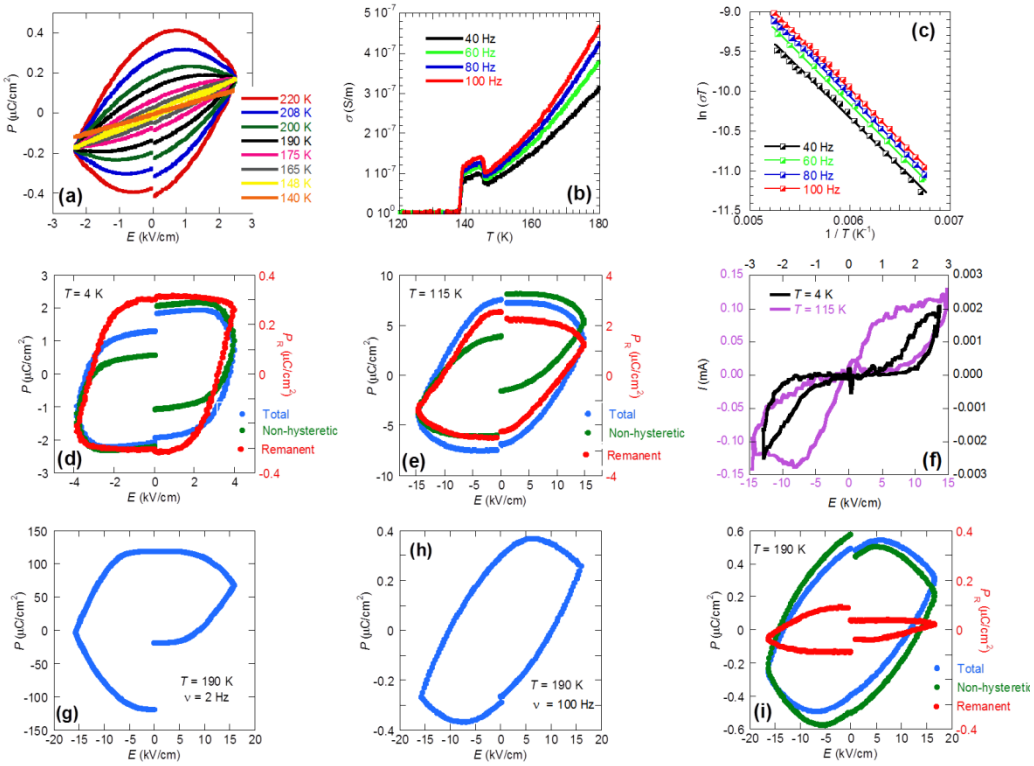

Fig. 1 Hysteresis loops of unpoled crystals. Top. (a) $P(E)$ hysteresis loops measured on cooling from room temperature through the cubic to tetragonal to orthorhombic transitions; the open lossy loop suddenly collapses at T_C^O . **(b)** AC conductivity σ_{AC} as a function of temperature for several low frequencies. **(c)** Modified Arrhenius plot showing linear behavior in the range 147 K < T < 195 K. **Middle (O-MAPB).** Remanent $P_R(E)$ loop (red), total (hysteretic plus non-hysteretic, blue) and non-hysteretic (green) $P(E)$ loops recorded at **(d)** 4 K and **(e)** 120 K after electric field pulses of 25 kV/cm for 0.5 sec. **(f)** Switching currents $I_R(E)$ of the $P_R(E)$ loops in **(d)** (black current) and **(e)** (purple current). **Bottom (T-MAPB).** $P(E)$ loop at 190 K measured at **(g)** 2 Hz and **(h)** 100 Hz, showing huge frequency dependence; **(i)** Remanent $P_R(E)$ loop (red), total (hysteretic plus non-hysteretic, blue) and non-hysteretic (green) $P(E)$ loops at 190 K and 100 Hz after electric field pulses, revealing a built-in permanently polarized state which, however, lacks ferroelectric features (in particular, switching is absent).

1f shows that switching is still barely visible (and if any only for one field polarity) at 120 K and 15 kV/cm (about ten times higher the value of the reported coercive field[52]).

The same procedure (i.e. cooling below T_C^T in zero electric field followed by electric field pulses) was thereafter applied to T-MAPB, with attention at using electric field intensity far below 30 kV/cm, to avoid irreversible sample degradation promoted by ions diffusion.[73–75] As shown in **Fig. 1g**, **h**, at 190 K $P(E)$ of T-MAPB has a strong dependence on the E_{AC} frequency, with maximum polarization value as high as 100 μC/cm^2 at 2 Hz.

A similar behavior - uncharacteristic of a ferroelectric response - was also reported for T-MAPI and shown to require a dominant non-ferroelectric process.[10] As electro-activated ions migration on mesoscopic or macroscopic distances in hybrid perovskites occurs on a timescale from milliseconds to seconds,[27,76,77] the low frequency high polarization is likely due to ion accumulation, in the same way as in T-MAPI under the effect of electric field pulses of comparable intensity and duration.[78] What is notable here is the non-vanishing $P_R(E)$ loop (cfr **Fig. 1i**), indicating that T-MAPB is brought by the electric field pulses into a permanently weakly polarized state: although the external electric field has been removed, the migrated ions have not been completely restored to the original uniform distribution state. We interpret the experiment as evidence for a ionic space-charge electret state. At 190 K, this field-induced metastable polarized state is only short lived and $P_R(E)$ decays rapidly to zero within several minutes.

Poled crystals. Poling in a DC electric field while cooling is a way to induce both space charge and dipolar electret states in dielectrics[55]. At the same time, if E_{DC} is larger than E_C, it is exactly the process used to polarize as-grown ferroelectrics. To

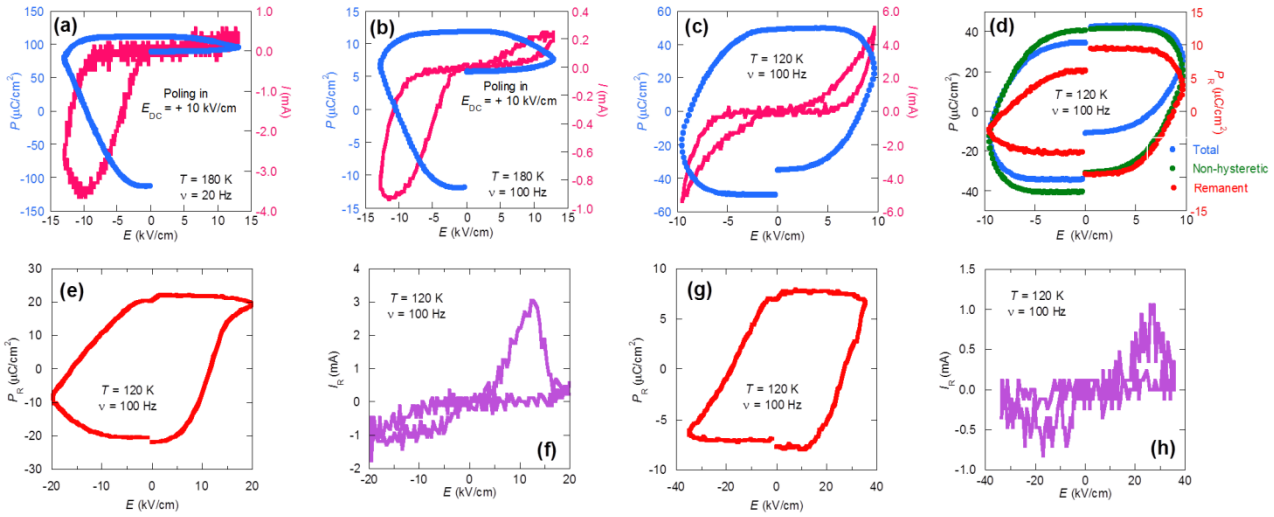

Fig. 2 Hysteresis loops of poled crystals. TOP: T-MAPB: $P(E)$ loop and switching current $I(E)$ at 180 K, measured at **(a)** 20 Hz and **(b)** 100 Hz after poling in +10 kV/cm from room temperature, followed by annealing at 180 K in the same field for further 30 min; **O-MAPB: (c)** $P(E)$ loop at 120 K after cooling in field from 180 K in +10 kV/cm and annealing for 30 minutes; **(d)** Remanent $P_R(E)$ loop (red), total (hysteretic plus non-hysteretic, blue) and non-hysteretic (green) $P(E)$ loops under the same condition of **(c)**; **BOTTOM: O-MAPB (e)** Remanent $P_R(E)$ loop at 120 K after further isothermal poling in +25 kV/cm for 10 min; **(f)** switching current $I_R(E)$ of the $P_R(E)$ loop shown in **(e)**. **(g)** Lozenge-type $P_R(E)$ loop obtained after several electric field application of both polarities starting from **(e); (h)** $I_R(E)$ current corresponding to the $P_R(E)$ loop of **(g).**

be poled, as-grown MAPB crystals were slowly cooled from room temperature in E_{DC} = +10 kV/cm. At 180 K, T-MAPB was isothermally annealed in field for additional 30 minutes, after which $P(E)$ and corresponding $I(E)$ loops were measured. Results are displayed in **Fig. 2a, b.** Ferroelectric-like $P(E)$ loops in poled T-MAPB were never measured. $P(E)$ loops were invariably gapped and polarization reached very high value at the lowest frequency, reflecting once more its space-charge origin.

Currents associated to $P(E)$ loops of poled T-MAPB are highly asymmetric: after positive E_{DC} poling, $I(E)$ has only a little variation in the positive E_{AC} quadrants. Thus, during poling migration of mobile charges creates a polarized state, in turn generating an internal electric field opposite to the poling one, preventing further ion accumulation. We note that charge injection would have facilitated current transport under forward bias after positive poling.[36] At 190 K, charges accumulated under forward bias seem not to be trapped, but instead almost free to follow the field when the sign of this latter is reversed. Analogous behavior takes place by poling in a negative E_{DC} = -10 kV/cm (see Supporting Information, **Figure S5 a, b**).

T-MAPB poled as described above (in E_{DC} = +10 kV/cm) was thereafter field-cooled to 120 K and annealed in field for additional 30 minutes. $P(E)$ and $P_R(E)$ loops of O-MAPB measured soon after this procedure are shown in **Fig. 2c**, **d**: they strongly resemble those obtained in unpoled crystals after electric field pulses (cfr **Fig. 1e**), however with maximum polarization about five times larger. That is to say, the loops of poled O-MAPB contain an excess remanent polarization which does not really belong to O-MAPB, but represents instead the frozen-in electret state of T-MAPB when it is cooled under E_{DC} through T_C^O. This state persisted overnight at 120 K without significant reduction.

The electric field has an impressive effect on the frozen-in electret state: further poling at 120 K for 10 minutes in a higher poling field of E_{DC} = +25 kV/cm provides us with a $P_R(E)$ loop which shows a clear switching in the positive E_{AC} quadrant (**Fig. 2e**); in correspondence, a marked peak is present in the $I_R(E)$ loop (**Fig. 2f**). The quite high $P_R(E)$ value (up to 20 μC/cm^2 at saturation) is unrealistic for a pure ferroelectric response of O-MAPB; the peculiarity of the $I_R(E)$ curve of **Fig. 2f** is rather indicative of an electric-field-induced resistive switching phenomenon, in which ferroelectricity may not even be involved. Actually, poling in 25 kV/cm for 10 minutes appears to have driven O-MAPB into a low resistance state which, at about +12 kV/cm, is reset to a high resistance state almost stable during the P_R(E) measurements in the negative E_{AC} quadrants. Resistive switching in insulating perovskites caused by ion-migration, connected to the formation and rupture of conductive filamentary paths under electric field, is well documented in both all-inorganic and hybrid halides perovskites.[52,79–82] The same asymmetric resistive switching can be observed when poling in negative E_{DC} fields (see Supporting Information, **Figure S5 c**, **d**). Overall, the combined effect of freezing by cooling and further poling in E_{DC} suppresses the resistive components of the short lived T-MAPB electret in favor of the stabilization of long lasting apacitive

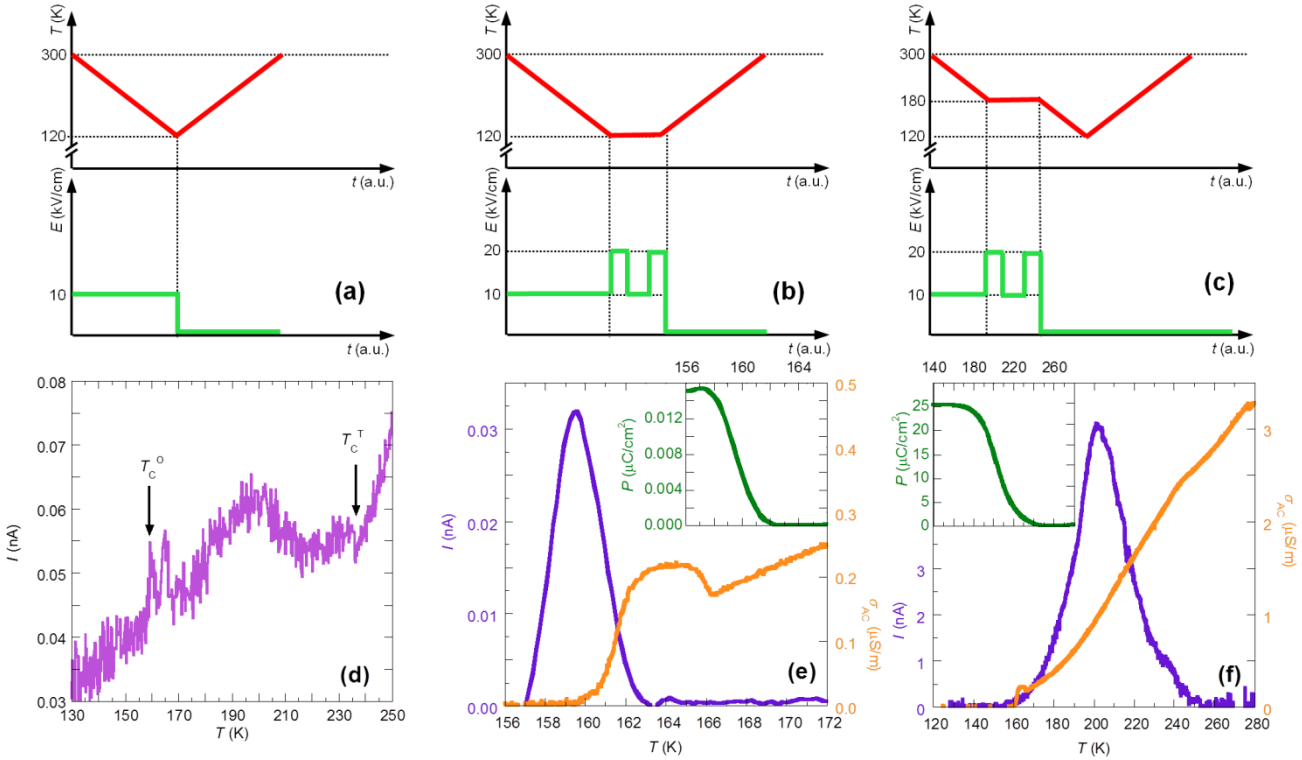

Fig. 3 Thermally stimulated discharge (o depolarization) current TSDC measured under different E_{DC}/T protocols. **(a)** *Protocol I*, during which a crystal was poled by cooling in E_{DC} = +10 kV/cm from room temperature to 120 K and short circuited for measuring TSDC on heating at 5 K/min. **(b)** *Protocol II*, used to separate, as far as possible, the response to E_{DC} pulses of poled O-MAPB from the electret-type polarization of T-MAPB; **(c)** *Protocol III*, used to isolate the response of T-MAPB and to study its depolarization after *i)* DC poling while cooling below T_C^T, *ii)* E_{DC} pulses, *iii)* freezing below T_C^O by zero-field-cooling. **(d)** TSDC after *Protocol I*, displaying small features at the structural phase transitions and a broad structure centered at 200 K. **(e)**: Current around T_C^O after *Protocol II*; **(f)** Current around T_C^T after *Protocol III* (Nb.: TSDC in **(e, f)** are shown after subtraction of the high temperature components by Gaussian deconvolution). Insets in **(e, f)** show the corresponding spontaneous polarizations. AC conductivity σ_{AC}(T) (in orange) in **(e, f)** evidences the structural phase transitions.

ones (i.e. ions becomes quasi permanently trapped). Finally, repeated manipulation of the poling field polarity produces an internal charge redistribution giving rise to a lozenge-shaped $P_R(E)$ loop (**Fig. 2g)** with slanted and almost parallel opposite sides, quite typical of electrets.[29] In this case only, an almost symmetric instantaneous current $I_R(E)$ loop was measured (**Fig. 2h**).

Thermally stimulated depolarization (or discharge) currents (TSDCs). In electrets, space charges are gradually set free on warming, while dipolar species that may have been oriented by the electric field (in this case MA^+ ions), if contributing to the metastable polarization, randomize. TSDC method consists in recording the associated temperature-dependent current development, while warming at a controlled heating rate a sample in parallel plate capacitor geometry, typically in zero electric field.

Different measuring protocols were applied to fresh-prepared MAPB single crystal, that were subjected to the combinations of poling E_{DC} field and electric field pulses shown in **Fig. 3a**-**c**. Apart from details concerning the intermediate phase (not discussed here), the whole experiment evidenced two main depolarization processes below T_C^T. The first one takes place sharply at T_C^O (**Fig. 3e**). If treated as the depolarization of a ferroelectric phase, it would correspond to a spontaneous polarization of only 0.015 μC/cm^2 at saturation (inset of **Fig. 3e**), even smaller than found by Gao et al..[52] The second process extends over the whole temperature stability range of T-MAPB, has its TSDC maximum at 200 K (**Fig. 3f**) and is strongly influenced by E_{DC} pulses applied to T-MAPB, which increase the current intensity by two orders of magnitudes with respect to poling alone, masking the small feature at T_C^T in **Fig. 3d**. This TSDC would correspond to *P* as high as 25 μC/cm^2 at saturation (inset of **Fig. 3f**), that again cannot be ascribed to ferroelectricity of T-MAPB: as recalled in the Introduction, such a large *P* would come from large polar atomic shifts in a non-centrosymmetric *I4cm* crystal structure which, however, did not show up in crystallographic investigations.[42]

The previous results can be discussed with reference to TSDCs measured in T-MAPI solar cells during identification of

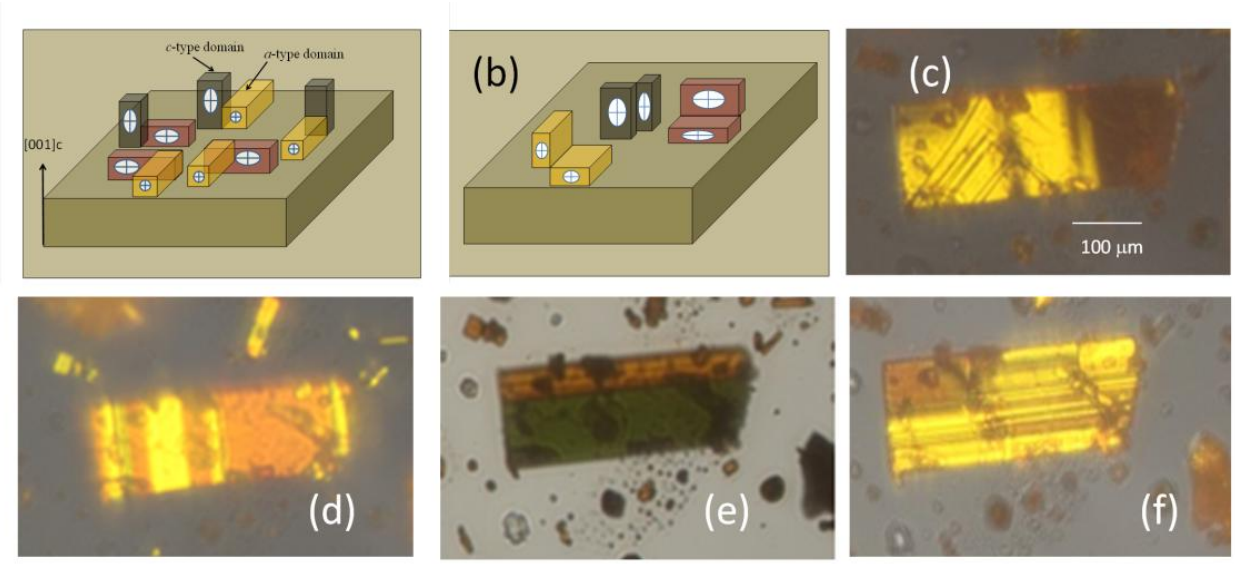

Fig. 4 (a, b) Sketched ferroelastic domains for T-MAPB and O-MAPB; *c*-type and *a*-type domains refer to domains with the unique tetragonal fourfold axis perpendicular or parallel to the $(001)_C$ crystal planes, respectively. The white small ellipses represent sections of the optical indicatrix. Ferroelastic domain structure at **(c)** 180 K and **(d, e, f)** 120 K observed in polarized light microscopy during three successive cooling cycles of a thin single crystal fragment. The observed lamella-like domains widths range between about 5 μm and 40 μm.

carrier traps filled under illumination.[75] In full correspondence to electrically poled MAPB single crystals, MAPI shows two main discharge peaks: a sharp one in coincidence with the tetragonal to orthorhombic transition, and a broad one within T-MAPI near 210 K (T_C^T of MAPI = 330 K). While the low temperature peak was at least partially put into relation with a not better-defined feature of the structural transition itself, the peak at 210 K was assigned to deep traps for photo-generated carriers with activation energy of about 500 meV. However, the recent literature on MAPI has unambiguously shown that illumination with energies above the gap increases both electronic and ionic conductivity by orders of magnitude, with a subtle mutual interplay.[27,85] An alternative interpretation can therefore be proposed and we assign the TSDC peak at 200 K of **Fig. 3f** to the depolarization of the ionic space-charge electret, with activation energy, evaluated by the initial rise method,[86] of 330 meV.

Theoretical simulations.

The low-intensity and sharp TSDC peak appearing at T_C^O is of more difficult interpretation. Actually, $P_R(E)$ loops that can be opened only by high electric field pulses as we showed in **Fig. 1 d**, **e** and the highly unusual asymmetric $I_R(E)$ loops (cfr **Fig. 1i** and **Fig. 2h, l**) work against ferroelectricity in O-MAPB. Moreover, we could not observe any second harmonic generation (SHG) from O-MAPB, that would have definitely proven the broken spatial inversion symmetry: we searched for it without success on grinded single crystals, sieved to two different micrometric grain sizes and pressed into pellets, according to the method of Kurtz & Perry[87] also used to probe SHG in tetragonal $CH_3NH_3PbI_3$;[45] given the sensitivity of our set-up, the upper limit for the efficiency of second harmonic conversion found at 80 K in O-MAPB could be placed 4 orders of magnitudes lower than the value for urea we employed as standard. Nevertheless, the presence of a depolarization process right at T_C^O, also showed by Gao et al.[52] and Bauman et al.[83] cannot be dismissed as a fortuitous coincidence.

To get more insight on the observed polarized state of O-MAPB, we performed atomistic simulations. We made use of a multi-scale approach with two different methods: (i) large-scale classical molecular dynamics simulations, under the working hypothesis that the mesoscopic crystallographic texture due to the ferroelastic character of the MAPB structural phase transitions may have a role in the formation of the electret states; (ii) *ab initio* first-principles calculations for a quantitative evaluation of the energetics of polar vs non polar structural configurations in O-MAPB.

Let us better specify point (i). As the crystal system changes at each structural transition, the non-cubic phases of MABP are ferroelastic. Ferroelasticity implies the reversible formation and dissolution, at the transition temperature, of ferroelastic domains and domain boundaries. During the sequence of symmetry breaking $m\bar{3}m$ to $\frac{4}{mmm}$ to mmm, four and six ferroelastic domains (differing for the spatial orientation of the strain tensor) can be generated in MAPB, as pictorially sketched in **Fig. 4a** and **Fig. 4b** for T-MAPB and O-MAPB respectively. Domains tiling in a specific crystal gives rise to a crystallographic domain structure organized on a

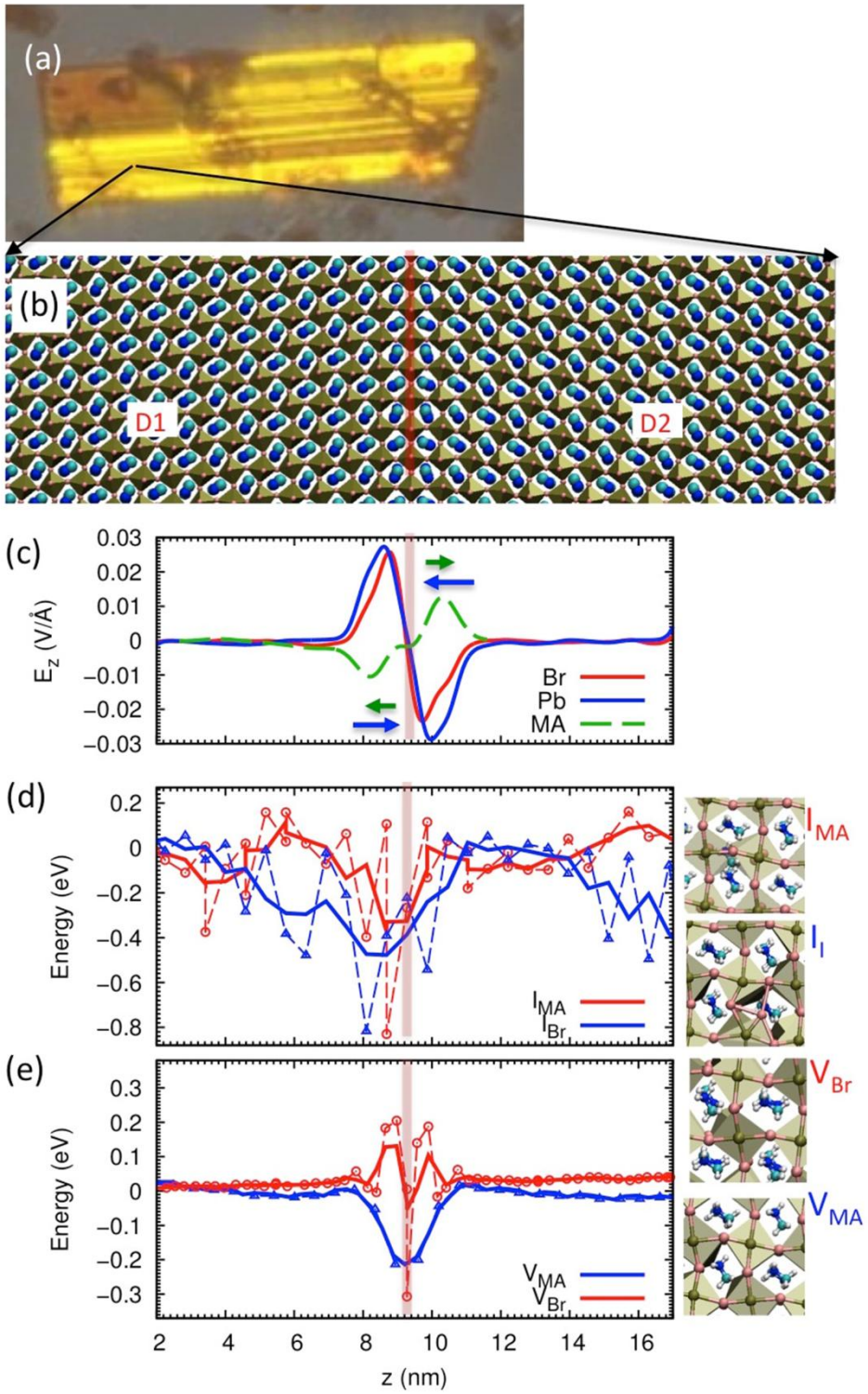

Fig. 5 (a) Ferroelastic domain structure optically observed in O-MAPB and **(b)** atomistic model of a $(110)_O$ twin mirror boundary between two ferroelastic domains; **(c)** Local electric field (lines) calculated at the position of Br (red), Pb (blue) atoms and MA molecule (green); arrows indicate the direction of the local electric field; **(d)** Energy of Br (blue) and MA (red) interstitials and **(e)** vacancy of Br (red) and MA (blue) as a function of the distance from the domain boundary. Lines are running averages that serve as guides for the eye. Right bottom insets represent the atomistic configurations of the point defects considered.

mesoscopic scale which can be directly observed in thin enough MAPB crystals. In **Fig. 4c** and **Fig. 4d**-**f** we report images we obtained by polarized light microscopy at 180 K and at 120 K, respectively.

Within the domain structure, ferroelastic domain boundaries - where the passage from the lattice orientation of one domain to the adjacent one takes place - are extended periodicity defects, the properties of which may be different from the bulk ones. Other extended defects, including surfaces,[71] hetero-interfaces, and grain boundaries,[88–90] act as traps for charged species in semiconductors and support concentrations of charge carriers and defects well above the bulk equilibrium value.[71,88] Analogously, ferroelastic domain boundaries of MAPB might interact with ionic point defects, thus playing a role on the electret formation.

To investigate this statement, we at first generated large atomistic models of ferroelastic domains. We used the MYP interatomic potential[91,92] extended to MAPB,[44] able to reproduce elastic, dielectric,[93] thermal properties and even degradation of hybrid perovskites.[94,95] We focused on the orthorhombic phase, whose *Pbnm* structure is well reproduced by the MYP model. We started from a crystalline slab-like domain D1 of *15* × *15* × *2* MAPB orthorhombic unit cells and cut along the $(110)_O$ crystallographic surface. A second domain D2 was generated by mirror-symmetry across the $(110)_O$ surface and merged to D1 with perfect Pb-Br bond-network matching at the interface. We modeled therefore a reflection twin in which the tetragonal mirror plane $(110)_T$ lost at the tetragonal to orthorhombic transition acts as twin law (domains in O-MAPB are shown again in **Fig. 5a**).[96] The final system contains 24576 atoms and its atomic forces are relaxed in periodic boundary conditions by optimizing volume and atomic positions through conjugate-gradient algorithm. The resulting atomistic model of the coherent $(110)_O$ boundary is displayed in **Fig. 5b**. Both domains preserve the original molecular ordering (though elastically distorted) corresponding to a tilting of 90° from each other.

Thereafter, we calculated the formation energy of four types of point defects (interstitials and vacancies of both methylammonium and bromide), generated, one at a time, at different distances from the boundary. Results for interstitials and vacancies are reported in **Fig. 5 (**Panel **d** and **e**, respectively). When the defect is far from the boundary, its formation energy tends to the bulk value, sets to zero. Let us first consider the positively charged MA vacancy, V_{MA}, (Panel **e**, blue line). The symmetric V_{MA} energy profile indicates a minor energy cost (~0.2 eV) for V_{MA} formation at the domain boundary rather than in the bulk. This implies that V_{MA} can be trapped at the boundary. The case of bromide vacancy V_{Br} corresponds to red points and red line of Panel **e**. The energy profile is still symmetric across the wall but nonmonotonic, with very sharp minimum indicating that the formation of V_{Br} at the boundary is by 0.3 eV more favorable than in the bulk. The energy cost necessary to release V_{Br} is even larger (about 0.5 eV) due to the occurrence of two barriers around the minimum. Finally, the cases of interstitials are reported in Panel **d** (blue and red are Br and MA interstitials, respectively). The energy profiles of interstitials, qualitatively different from vacancies, show larger fluctuations in energy, deeper (larger than 0.6 eV) and much broader absolute minima, which are shifted (within 2 nm) with respect to the domain boundary. Overall, the results indicate that all the investigated defects tend to be more abundant close to the boundary.

To get physical insight in the above results we calculated the averaged electric field at the positions of Br, Pb and MA, reported in Panel **e** of **Fig. 5** as a function of the distance from the domain boundary (blue, red, green curves, respectively for the mentioned three atomic species). The electric field, zero everywhere but for an oscillation centered at the boundary, indicates a local dipolar field at the boundary itself with no net charge, as expected from the mirror symmetry. The electric field on Pb and Br and on MA has opposite sign. The former (blue arrows) confines positive V_{Br} at the center of the boundary, while shifting negative I_{Br} out of the center. For MA the electric field is reversed (green arrow), and negative V_{MA} are pushed towards the boundary. These findings are consistent with the energetics of defects, while the residual elastic strain within the system can explain the long-range energy variations calculated for interstitials, quite sizable within 4-5 nanometers from the boundary. The above analysis provides clear evidence that the domain boundary perturbs the population of defects favoring the formation of defects close to boundary with an energy gain of 0.2 eV-0.5 eV for vacancies and up to 0.8 eV for interstitials.

The present results provides a vivid proof of the efficiency of domain boundaries in the stabilization of the MAPB electret when cooling down to the orthorhombic phase. Moreover, the dissolution/formation of such internal homo-interfaces while warming and cooling through T_C^O will give rise to a net current flow at the transition, generated by ionic motion toward and forward the boundary itself in concomitance with the steplike change of mobility and spontaneous strain release/unrelease.

To explore instead the possibility of some genuine, long-range ferroelectric order below T_C^O, where the electret does not form owing to the reduced ionic mobility, we performed first-principles calculations. To the aim, having fixed the orthorhombic $\sqrt{2}a_c \times \sqrt{2}a_c \times 2a_c$ unit cell parameters *a*, *b*, *c* (common to centric *Pbnm* and acentric $Pbn2_1$ structures) to those indicated by the experiments[38,42], we considered all the possible orientations of the four MA molecules included in the cell. For each configuration, starting from trial atomic positions, we relaxed the structure to reach a stable local minimum, a strategy used in the past for $MAPbI_3$.[97] At the end, we are left with about 60 nonequivalent configurations, covering an energy range ~ 120 meV/f.u., thus separated, on average, by just 2 meV/f.u. from each other. The smallness of this energy difference indicates that we cannot limit the computational analysis to a handful of significant structures (i.e. the parent paraelectric and a few derived polar phases), as for conventional ferroelectrics; instead, the full landscape of metastable, tightly competing microstates compatible with the orthorhombic unit cell must be considered.

Fig. 6a displays the calculated total energy for each of the obtained 60 static local minima, and **Fig. 6b**, **c** the

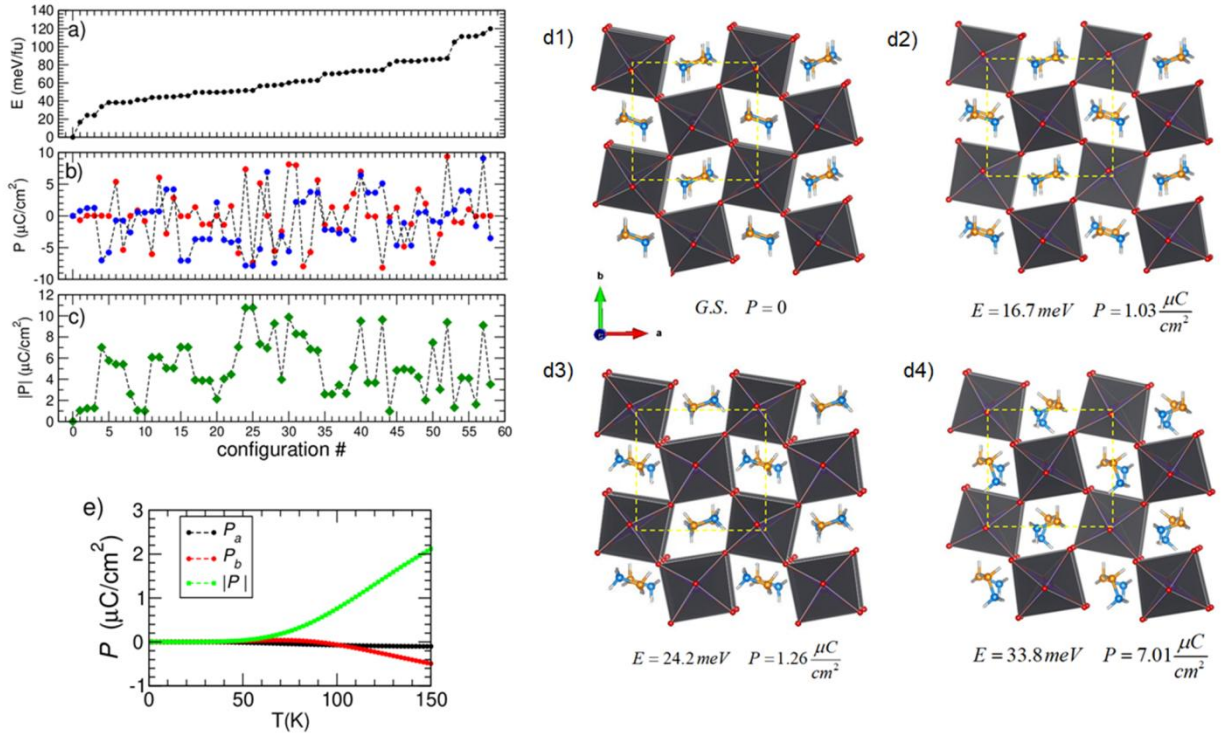

Fig. 6 (a) Calculated energies for the 60 distinct metastable configurations in O-MAPB. **(b)** Calculated components of spontaneous polarization along axis *a* (red circles) and *b* (blue circles) of the *Pbnm* orthorhombic cell, corresponding to [110] and [1$\underline{1}$0] cubic directions. **(c)** The corresponding polarization modulus for the same structures. **(d)** The calculated atomic structures (view along *c*, i.e. the cubic [001] direction) of the four energy lowest configurations; d1 is the absolute ground-state (configuration '0' in **Figs. 5a**, **5b**, **5c**) with P = 0; **d2**, **d3** and **d4** are the three nearest metastable states with not vanishing polarization; energies and polarization are reported for each of those. **(e)** Polarization as a function of temperature, obtained as Boltzmann thermal average over the 60 metastable configurations.

corresponding spontaneous polarization calculated by the Berry phase approach. The crystal structures of the four lowest energies are drawn in **Fig. 6d**. The ground state structure (configuration '0') shows a vanishing polarization within the resolution limits fixed by our numerical accuracy (i.e. P lower than 0.01 μC/cm^2). This state is 16 meV/f.u. more stable than any other local minimum, then it largely dominates the low-temperature behavior. From **Fig. 6d1** we see that configuration '0' has MA$^+$ dipoles compensating along *a* but not along *b* (corresponding to cubic [110] and [1$\underline{1}$0]). The not vanishing *b*-axis polarization, however, is visibly compensated by the analogous but verse-inverted orientation of the dipoles in the adjacent (*a*,*b*) plane. he ground state appears therefore anti-ferroelectric, with in-plane polarization directed along *b* and stacked along *c* (corresponding to cubic[001]) with alternating verse, in agreement with the experimental *Pbnm* crystal structure[41,42] and consistent with the minimum energy molecular orientation predicted by classical force-fields.[44]

Above in energy, in the range between 16 and 33 meV/f.u. from state '0', we found three metastable states with moderate P_b ~1-2 μC/cm^2 and very marginal P_a (see their corresponding atomic structures in **Fig. 6d2**-**d4**). In is worth noticing that the calculated polarization, mainly resulting from uncompensated plane-by-plane MA$^+$ dipole alignment, also contain a contribution from Pb off-centering and octahedral stretching, due to the tight coupling between organic and inorganic sublattices at low temperature.

Going upper in energy, we find several local structures with quite significant polarization, in the range P ~5-10 μC/cm^2 which, however, is largely averaged out in the (*a*,*b*) plane. As an estimate of the configurationally averaged spontaneous polarization at a finite temperature, we considered the Boltzmann thermal averages of P_a, P_b and absolute P amplitude, reported in **Fig. 6e** up to T_C^O. We see that the non-polar state '0' pinches the polarization to zero up to T ~ 50 K. Thereafter, the higher energy minima start to contribute; nevertheless, while the non-observable P amplitude reaches significant values (~2 μC/cm^2 for T = 150 K) P_a and P_b remains marginal, with P_b ~0.1-0.4 μC/cm^2 and virtually vanishing P_a.

The previous scenario is similar to that depicted for MAPI in Ref.[97] where it was also found that configurational entropy is strongly effective in suppressing any long-range order

ferroelectricity. We remark that at variance with MAPI, for O-MAPB we find a robust non-polar (or anti-ferroelectric) ground state. Finally, it is natural to wonder whether the metastable polar states described above could be instrumental to explain the hysteresis loops shown by as-grown and poled O-MAPB crystals (cfr **Fig. 1e** and **Fig. 2d**, **e**, **g**), envisioning a situation where the application of electric field may project the crystal onto one, or a few, specifically polarized metastable states. That is to say, the metastable electret might contain a dipolar contribution from MA molecules not participating to ionic conduction but bound to the crystal structure, with the growth of some polarized domains under electric field. This would be appealing, as it is reminiscent of the electric field induced paraelectric to ferroelectric transition in relaxors, materials that also contains polar nanodomains that may merge under the effect of electric field.[98] However, the idea collides with the relatively small (order of 50 meV[44,91,99]) energy cost for rotation of MA molecules and, by consequence, with the easiness of switching among different metastable domains, as the ones shown in **Fig. 6,** which would prevent long lived macroscopic polarized states. Thus we can quite safely conclude that the long-living electret states herewith observed in O-MAPB are better explained in terms of trapping of ionic charges.

Conclusions

In this work we explored the electric polarization of hybrid perovskite $CH_3NH_3PbBr_3$ in its non cubic phases. In all the analyzed crystals we observed field-induced metastable electrets and lack of spontaneous polarization. Our proposed scenario is that a short-lived electret state is formed in the good ionic conductor T-MAPB likely due to the interaction of mobile ionic defects with ferroelastic domain boundaries and that this state can be frozen, under electric field cooling, into the poorly ionic conductive O-MAPB, to produce a long-lasting polarization below 145 K. For what concerns long-range ferroelectric behavior at low temperature, our calculations indicate that the net polarization is averaged away by the large number of competing metastable polar states resulting from the different MA sublattice configurations compatible with the O-MAPB structure. Our results highlight the two most important features preventing the development of long-range ferroelectric order in 3D lead based hybrid perovskites: i) the high ionic conductivity produced by Br^-, MA^+ and Pb^{2+} long-range hopping, which is clearly antithetic to the off-centered switching giving rise to ferroelectricity; ii) the large configurational entropy due to a plethora of metastable states with differently oriented polarization, which contrasts the dominance of a specifically polarized ground state.

Such a complex scenario also motivates the large variety of results emerging from the literature. In fact, it is not difficult to figure out a situation where highly pure samples, under the action of strong field, could manifest some ferroelectric hysteresis, before that degradation processes takes place, with consequent defects formation. It is perhaps this "one shot" ferroelectricity that has been reported by Gao et al..[52] Our study draws attention to the central role of ionic conduction, ferroelastic domains, and configurational entropy in the electric behavior of this fascinating class of materials.

Conflicts of interest

There are no conflicts to declare.

Acknowledgements

A. M. acknowledges MIUR for funding though project PON04a2 00490) “M2M Netergit” and PRACE for awarding him access to Marconi KNL at CINECA, Italy, through projects DECONVOLVES (2018184466) and PROVING-IL (2019204911).
We acknowledge the CeSAR (Centro Servizi d'Ateneo per la Ricerca) of the University of Cagliari, Italy for the dielectric constant and specific heat measurements performed with the Quantum Design PPMS DynaCool and for the X-ray powder diffraction patterns collected on the Bruker D8 Advance Diffractometer.

References

1 A. Kojima, K. Teshima, Y. Shirai and T. Miyasaka, *J. Am. Chem. Soc.*, 2009, **131**, 6050–6051.
2 V. M. Fridkin, *Crystallogr. Reports*, 2001, **46**, 722–726.
3 J. Kreisel, M. Alexe and P. A. Thomas, *Nat. Mater.*, 2012, **11**, 260.
4 K. T. Butler, J. M. Frost and A. Walsh, *Energy Environ. Sci.*, 2015, **8**, 838–848.
5 H. S. Kim and N. G. Park, *J. Phys. Chem. Lett.*, 2014, **5**, 2927–2934.
6 C. Li, S. Tscheuschner, F. Paulus, P. E. Hopkinson, J. Kießling, A. Köhler, Y. Vaynzof and S. Huettner, *Adv. Mater.*, 2016, **28**, 2446–2454.
7 C. Li, A. Guerrero, Y. Zhong and S. Huettner, *J. Phys. Condens. Matter*, 2017, **29**, 193001.
8 J. M. Frost, K. T. Butler and A. Walsh, *APL Mater.*, 2014, **2**, 081506.
9 J. Wei, Y. Zhao, H. Li, G. Li, J. Pan, D. Xu, Q. Zhao and D. Yu, *J. Phys. Chem. Lett.*, 2014, **5**, 3937–3945.
10 J. Beilsten-Edmands, G. E. Eperon, R. D. Johnson, H. J. Snaith and P. G. Radaelli, *Appl. Phys. Lett.*, 2015, **106**, 173502.
11 Z. Fan, J. Xiao, K. Sun, L. Chen, Y. Hu, J. Ouyang, K. P. Ong, K. Zeng and J. Wang, *J. Phys. Chem. Lett.*, 2015, **6**, 1155–1161.
12 S. Meloni, T. Moehl, W. Tress, M. Franckeviius, M. Saliba, Y. H. Lee, P. Gao, M. K. Nazeeruddin, S. M. Zakeeruddin, U. Rothlisberger and M. Graetzel, *Nat. Commun.*, 2016, **7**, 10334.
13 P. Calado, A. M. Telford, D. Bryant, X. Li, J. Nelson, B. C. O’Regan and P. R. F. Barnes, *Nat. Commun.*, 2016, **7**, 1–10.
14 P. Delugas, C. Caddeo, A. Filippetti and A. Mattoni, *J. Phys. Chem. Lett.*, 2016, **7**, 2356–2361.
15 J. Seidel, D. Fu, S. Y. Yang, E. Alarcón-Lladó, J. Wu, R. Ramesh and J. W. Ager, *Phys. Rev. Lett.*, 2011, **107**, 1–4.
16 S. Y. Yang, J. Seidel, S. J. Byrnes, P. Shafer, C.-H. Yang, M. D.

Rossell, P. Yu, Y.-H. Chu, J. F. Scott, J. W. Ager, L. W. Martin and R. Ramesh, *Nat. Nanotechnol.*, 2010, **5**, 143–147.
17 S. Liu, F. Zheng, N. Z. Koocher, H. Takenaka, F. Wang and A. M. Rappe, *J. Phys. Chem. Lett.*, 2015, **6**, 693–699.
18 S. N. Rashkeev, F. El-Mellouhi, S. Kais and F. H. Alharbi, *Sci. Rep.*, 2015, **5**, 1–8.
19 T. S. Sherkar and L. Jan Anton Koster, *Phys. Chem. Chem. Phys.*, 2016, **18**, 331–338.
20 Y. Kutes, L. Ye, Y. Zhou, S. Pang, B. D. Huey and N. P. Padture, *J. Phys. Chem. Lett.*, 2014, **5**, 3335–3339.
21 H. S. Kim, S. K. Kim, B. J. Kim, K. S. Shin, M. K. Gupta, H. S. Jung, S. W. Kim and N. G. Park, *J. Phys. Chem. Lett.*, 2015, **6**, 1729–1735.
22 G. Sharada, P. Mahale, B. P. Kore, S. Mukherjee, M. S. Pavan, C. De, S. Ghara, A. Sundaresan, A. Pandey, T. N. Guru Row and D. D. Sarma, *J. Phys. Chem. Lett.*, 2016, **7**, 2412–2419.
23 P. Wang, J. Zhao, L. Wei, Q. Zhu, S. Xie, J. Liu, X. Meng and J. Li, *Nanoscale*, 2017, **9**, 3806–3817.
24 M. Sajedi Alvar, M. Kumar, P. W. M. Blom, G. J. A. H. Wetzelaer and K. Asadi, *AIP Adv.*, 2017, **7**, 095110.
25 Y. Rakita, O. Bar-Elli, E. Meirzadeh, H. Kaslasi, Y. Peleg, G. Hodes, I. Lubomirsky, D. Oron, D. Ehre and D. Cahen, *Proc. Natl. Acad. Sci. U. S. A.*, 2017, **114**, E5504–E5512.
26 H. Röhm, T. Leonhard, A. D. Schulz, S. Wagner, M. J. Hoffmann and A. Colsmann, *Adv. Mater.*, , DOI:10.1002/adma.201806661.
27 Y. C. Zhao, W. K. Zhou, X. Zhou, K. H. Liu, D. P. Yu and Q. Zhao, *Light Sci. Appl.*, 2017, **6**, e16243-8.
28 D. Głowienka, T. Miruszewski and J. Szmytkowski, *Solid State Sci.*, 2018, **82**, 19–23.
29 J. F. Scott and J. Gardner, *Mater. Today*, 2018, **21**, 553–562.
30 Y. Liu, L. Collins, R. Proksch, S. Kim, B. R. Watson, B. Doughty, T. R. Calhoun, M. Ahmadi, A. V. Ievlev, S. Jesse, S. T. Retterer, A. Belianinov, K. Xiao, J. Huang, B. G. Sumpter, S. V. Kalinin, B. Hu and O. S. Ovchinnikova, *Nat. Mater.*, 2018, **17**, 1013–1019.
31 A. D. Schulz, H. Röhm, T. Leonhard, S. Wagner, M. J. Hoffmann and A. Colsmann, *Nat. Mater.*, 2019, **18**, 1050.
32 H. Cho, S. H. Jeong, M. H. Park, Y. H. Kim, C. Wolf, C. L. Lee, J. H. Heo, A. Sadhanala, N. S. Myoung, S. Yoo, S. H. Im, R. H. Friend and T. W. Lee, *Science (80-.).*, 2015, **350**, 1222–1225.
33 D. P. McMeekin, G. Sadoughi, W. Rehman, G. E. Eperon, M. Saliba, M. T. Hörantner, A. Haghighirad, N. Sakai, L. Korte, B. Rech, M. B. Johnston, L. M. Herz and H. J. Snaith, *Science (80-.).*, 2016, **351**, 151–155.
34 G. E. Eperon, M. T. Hörantner and H. J. Snaith, *Nat. Rev. Chem.*, 2017, **1**, 0095.
35 D. Marongiu, X. Chang, V. Sarritzu, N. Sestu, R. Pau, A. Geddo Lehmann, A. Mattoni, F. Quochi, M. Saba, A. Mura and G. Bongiovanni, *ACS Energy Lett.*, 2017, **2**, 769–775.
36 P. Andričević, X. Mettan, M. Kollár, B. Náfrádi, A. Sienkiewicz, T. Garma, L. Rossi, L. Forró and E. Horváth, *ACS Photonics*, 2019, **6**, 967–975.
37 J. Zhang and W. Li, in *Perovskite Materials, Devices and Integration*, ed. H. Tian, IntechOpen, 2020, vol. i.
38 A. Poglitsch and D. Weber, *J. Chem. Phys.*, 1987, **87**, 6373–6378.
39 Y. Guo, O. Yaffe, D. W. Paley, A. N. Beecher, T. D. Hull, G. Szpak, J. S. Owen, L. E. Brus and M. A. Pimenta, *Phys. Rev. Mater.*, 2017, **1**, 1–6.
40 C. A. López, M. C. Alvarez-Galván, M. V. Martínez-Huerta, F. Fauth and J. A. Alonso, *CrystEngComm*, 2020, **22**, 767–775.
41 I. P. Swainson, R. P. Hammond, C. Soullière, O. Knop and W. Massa, *J. Solid State Chem.*, 2003, **176**, 97–104.
42 H. Mashiyama and Y. Kawamura, 2006, **51**, 15–17.
43 N. Onoda-Yamamuro, T. Matsuo and H. Suga, *J. Phys. Chem. Solids*, 1992, **53**, 935–939.
44 T. Hata, G. Giorgi, K. Yamashita, C. Caddeo and A. Mattoni, *J. Phys. Chem. C*, 2017, **121**, 3724–3733.
45 S. Govinda, B. P. Kore, M. Bokdam, P. Mahale, A. Kumar, S. Pal, B. Bhattacharyya, J. Lahnsteiner, G. Kresse, C. Franchini, A. Pandey and D. D. Sarma, *J. Phys. Chem. Lett.*, 2017, **8**, 4113–4121.
46 P. Singh, C. Upadhyay, Z. Konôpková, H. P. Liermann and D. Pandey, *Phys. Rev. Mater.*, 2019, **3**, 1–11.
47 A. I. Lebedev, *Phys. Solid State*, 2009, **51**, 802–809.
48 P. H. Sun, T. Nakamura, Y. J. Shan, Y. Inaguma and M. Itoh, *Ferroelectrics*, 1998, **217**, 137–145.
49 J. Breternitz, F. Lehmann, S. A. Barnett, H. Nowell and S. Schorr, *Angew. Chemie - Int. Ed.*, 2020, **59**, 424–428.
50 Y. Rakita, E. Meirzadeh, T. Bendikov, V. Kalchenko, I. Lubomirsky, G. Hodes, D. Ehre and D. Cahen, *APL Mater.*, 2016, **4**, 051101.
51 S. Govinda, B. P. Kore, P. Mahale, A. Pandey and D. D. Sarma, *ACS Energy Lett.*, 2018, **3**, 1887–1891.
52 Z. R. Gao, X. F. Sun, Y. Y. Wu, Y. Z. Wu, H. L. Cai and X. S. Wu, *J. Phys. Chem. Lett.*, 2019, **10**, 2522–2527.
53 H. Yan, T. Ou, H. Jiao, T. Wang, Q. Wang, C. Liu, X. Liu, Y. Han, Y. Ma and C. Gao, *J. Phys. Chem. Lett.*, 2017, **8**, 2944–2950.
54 O. Heaviside, *Electrical Papers, Vol. I*, Macmillan, London, 1892.
55 V. N. Kestelman, L. S. Pinchuk and V. A. Goldade, *Electrets In Engineering*, Springer US, Boston, MA, 2000.
56 V. Leonov and C. Van Hoof, *Smart Mater. Res.*, 2012, **2012**, 1–9.
57 E. M. Panchenko, O. I. Prokopalo, A. E. Panich, V. A. Zagoruiko and Y. A. Trusov, *J. Phys. D. Appl. Phys.*, 1989, **22**, 1372–1374.
58 Y. J. Kim and C. H. Yang, *NPG Asia Mater.*, 2020, **12**, 1–9.
59 J. N. Wilson, J. M. Frost, S. K. Wallace and A. Walsh, *APL Mater.*, 2019, **7**, 010901.
60 M. I. Saidaminov, A. L. Abdelhady, B. Murali, E. Alarousu, V. M. Burlakov, W. Peng, I. Dursun, L. Wang, Y. He, G. MacUlan, A. Goriely, T. Wu, O. F. Mohammed and O. M. Bakr, *Nat. Commun.*, 2015, **6**, 1–6.
61 S. Plimpton, *J. Comput. Phys.*, 1995, **117**, 1–19.
62 P. Giannozzi, S. Baroni, N. Bonini, M. Calandra, R. Car, C. Cavazzoni, D. Ceresoli, G. L. Chiarotti, M. Cococcioni, I. Dabo, A. Dal Corso, S. De Gironcoli, S. Fabris, G. Fratesi, R. Gebauer, U. Gerstmann, C. Gougoussis, A. Kokalj, M. Lazzeri, L. Martin-Samos, N. Marzari, F. Mauri, R. Mazzarello, S. Paolini, A. Pasquarello, L. Paulatto, C. Sbraccia, S. Scandolo, G. Sclauzero, A. P. Seitsonen, A. Smogunov, P. Umari and R. M. Wentzcovitch, *J. Phys. Condens. Matter*, 2009, **21**, 395502.
63 D. Vanderbilt, *Phys. Rev. B*, 1990, **41**, 7892–7895.
64 A. Filippetti and A. Mattoni, *Phys. Rev. B*, 2014, **89**, 125203.
65 A. Filippetti, P. Delugas and A. Mattoni, *J. Phys. Chem. C*, 2014, **118**, 24843–24853.
66 P. Delugas, A. Filippetti and A. Mattoni, *Phys. Rev. B*, 2015, **92**, 045301.

67 R. D. King-Smith and D. Vanderbilt, *Phys. Rev. B*, 1993, **47**, 1651–1654.
68 J. T. Evans, Characterizing Ferroelectric Materials, https://www.ferrodevices.com/1/297/files/Ferroelectric_Properties_and_Instrumentation(1).pdf.
69 A. J. Joseph and B. Kumar, *Solid State Commun.*, 2018, **271**, 11–15.
70 J. F. Scott, *J. Phys. Condens. Matter*, 2008, **20**, 21–23.
71 C. Caddeo, A. Filippetti and A. Mattoni, *Nano Energy*, 2020, **67**, 104162.
72 J. M. Azpiroz, E. Mosconi, J. Bisquert and F. De Angelis, *Energy Environ. Sci.*, 2015, **8**, 2118–2127.
73 Y. Yuan, Q. Wang, Y. Shao, H. Lu, T. Li, A. Gruverman and J. Huang, *Adv. Energy Mater.*, 2016, **6**, 1–7.
74 B. Xu, W. Wang, X. Zhang, H. Liu, Y. Zhang, G. Mei, S. Chen, K. Wang, L. Wang and X. W. Sun, *Sci. Rep.*, 2018, **8**, 1–7.
75 V. Prakasam, D. Tordera, H. J. Bolink and G. Gelinck, *Adv. Opt. Mater.*, 2019, **7**, 1–7.
76 Y. Zhao, C. Liang, H. Zhang, D. Li, D. Tian, G. Li, X. Jing, W. Zhang, W. Xiao, Q. Liu, F. Zhang and Z. He, *Energy Environ. Sci.*, 2015, **8**, 1256–1260.
77 S. Chen, X. Wen, R. Sheng, S. Huang, X. Deng, M. A. Green and A. Ho-Baillie, *ACS Appl. Mater. Interfaces*, 2016, **8**, 5351–5357.
78 M. H. Futscher, J. M. Lee, L. McGovern, L. A. Muscarella, T. Wang, M. I. Haider, A. Fakharuddin, L. Schmidt-Mende and B. Ehrler, *Mater. Horizons*, 2019, **6**, 1497–1503.
79 R. Waser and M. Aono, *Nat. Mater.*, 2007, **6**, 833–840.
80 X. Guan, W. Hu, M. A. Haque, N. Wei, Z. Liu, A. Chen and T. Wu, *Adv. Funct. Mater.*, 2018, **28**, 1–11.
81 H. Ma, W. Wang, H. Xu, Z. Wang, Y. Tao, P. Chen, W. Liu, X. Zhang, J. Ma and Y. Liu, *ACS Appl. Mater. Interfaces*, 2018, **10**, 21755–21763.
82 B. Li, W. Hui, X. Ran, Y. Xia, F. Xia, L. Chao, Y. Chen and W. Huang, *J. Mater. Chem. C*, 2019, **7**, 7476–7493.
83 A. Baumann, S. Väth, P. Rieder, M. C. Heiber, K. Tvingstedt and V. Dyakonov, *J. Phys. Chem. Lett.*, 2015, **6**, 2350–2354.
84 C. Qin, T. Matsushima, T. Fujihara, W. J. Potscavage and C. Adachi, *Adv. Mater.*, 2016, **28**, 466–471.
85 G. Y. Kim, A. Senocrate, T. Y. Yang, G. Gregori, M. Grätzel and J. Maier, *Nat. Mater.*, 2018, **17**, 445–449.
86 G. F. J. Garlick and A. F. Gibson, *Proc. Phys. Soc.*, 1948, **60**, 574–590.
87 S. K. Kurtz and T. T. Perry, *J. Appl. Phys.*, 1968, **39**, 3798–3813.
88 N. Phung, A. Al-Ashouri, S. Meloni, A. Mattoni, S. Albrecht, E. L. Unger, A. Merdasa and A. Abate, *Adv. Energy Mater.*, 2020, **10**, 1903735.
89 A. Mattoni and S. Meloni, *Helv. Chim. Acta*, 2020, **103**, e2000110.
90 J. S. Park, J. Calbo, Y. K. Jung, L. D. Whalley and A. Walsh, *ACS Energy Lett.*, 2019, **4**, 1321–1327.
91 A. Mattoni, A. Filippetti, M. I. Saba and P. Delugas, *J. Phys. Chem. C*, 2015, **119**, 17421–17428.
92 A. Mattoni, A. Filippetti, M. I. Saba, C. Caddeo and P. Delugas, *J. Phys. Chem. Lett.*, 2016, **7**, 529–535.
93 A. Mattoni and C. Caddeo, *J. Chem. Phys.*, , DOI:10.1063/1.5133064.
94 C. Caddeo, C. Melis, M. I. Saba, A. Filippetti, L. Colombo and A. Mattoni, *Phys. Chem. Chem. Phys.*, 2016, **18**, 24318–24324.
95 C. Caddeo, M. I. Saba, S. Meloni, A. Filippetti and A. Mattoni, *ACS Nano*, 2017, **11**, 9183–9190.
96 Y. Wang and R. Liebermann, *Phys. Chem. Miner.*, 1993, **20**, 147–158.
97 A. Filippetti, P. Delugas, M. I. Saba and A. Mattoni, *J. Phys. Chem. Lett.*, 2015, **6**, 4909–4915.
98 A. A. Bokov and Z. G. Ye, *J. Mater. Sci.*, 2006, **41**, 31–52.
99 C. Motta, F. El-Mellouhi and S. Sanvito, *Phys. Rev. B*, 2016, **93**, 1–7.